*Bull. Mater. Sci.* (2023) 46:155
https://doi.org/10.1007/s12034-023-02993-5



# Tunable blue–green emission properties of $Tb^{3+}$ doped barium tantalate phosphor

**METE KAAN EKMEKÇİ***
Faculty of Science, Department of Chemistry, Marmara University, Göztepe Campus, 34722 İstanbul, Turkey
*Author for correspondence (mekmekci@marmara.edu.tr)

MS received 21 October 2022; accepted 24 April 2023

**Abstract.** The TTB (tetragonal tungsten bronze) crystal structure with the general formula of $A_4B_2C_4M_{10}O_{30}$ has three tunnels (A, B, C) of different coordination numbers with a corner-shared octahedral formation. Thanks to these properties, the TTB structure enables various RE ion substitutions and different physical properties to emerge. A series of green-emitting $Tb^{3+}$ doped barium tantalate phosphors with TTB-type structure between 0.25 and 5 mol% obtained by the solid-state reaction route is reported. The structure of $Tb^{3+}$ doped TTB–$BaTa_2O_6$ was identified by XRD and SEM-EDS analyses. PL relative emission intensity increased from 0.25 to 0.5 mol% and then decreased due to concentration quenching. Depending on the increasing concentration, the colour of the luminescence of $BaTa_2O_6$:$Tb^{3+}$ phosphor can be tuned from blue to green through a cross-relaxation process, where a dipole–dipole energy transfer occurs between two nearby $Tb^{3+}$ ions. The PL emission of the $BaTa_2O_6$:$Tb^{3+}$ in the CIE diagram tended towards blue to green with the increase in $Tb^{3+}$ concentration. PL decay profiles of the $^5D_3$ and $^5D_4$ states have a double exponential. The observed lifetimes of the $^5D_3$ state decrease as the decay profiles of the $^5D_4$ state exhibit a stable tendency. Based on the cross-relaxation process, the quantum efficiency ($\eta_{QE}$) of the phosphor was evaluated, and the $\eta_{QE}$ of the $^5D_3$ state with the increase of $Tb^{3+}$ concentration between 0.25 and 5 mol% varied from 61.63 to 40.85%, respectively.

**Keywords.** $Tb^{3+}$ doping; decay time; luminescence; colour tunable phosphor.

## 1. Introduction

Advances in optical material technology have made rapid progress over the past few decades. Among the functional materials, trivalent rare earth (RE: $Eu^{3+}$, $Dy^{3+}$, $Tb^{3+}$, etc.) metal-doped luminescent materials are very important owing to their versatile technological use in many fields, such as electroluminescent and fluorescent technology, screen technology, the novel lighting technology or W-LEDs, biomedical diagnosis applications, lasers, optical storage systems, laser spectroscopy and optical-fibre amplifiers [1–7]. In general, the trivalent terbium ($Tb^{3+}$) ion emits in the green under the excitation of different radiation sources [such as X-ray and ultraviolet (UV)] when doped to different host matrices [8–11]. The green emissions of $Tb^{3+}$ doped phosphors are sourced from $^5D_4$–$^7F_J$ transitions (J = 0, 1, 2, 3, 4, 5, 6). Besides $^5D_4$ green emissions, $^5D_3$ blue emissions can be observed, which depend on the phonon spectrum of the host structure and the $Tb^{3+}$ doping concentration [10–20]. Blue emissions of $Tb^{3+}$ will become evident, as the host structure with low phonon frequency and low $Tb^{3+}$ concentrations will suppress multiphonon relaxation and cross-relaxation between $Tb^{3+}$ ions. Therefore, different emission colours of $Tb^{3+}$ doped phosphors can be obtained by choosing a proper host lattice and suitable concentrations of $Tb^{3+}$ [10–20].

$BaTa_2O_6$ has three crystal structures, namely orthorhombic, hexagonal and tetragonal, the latter of which exhibits tungsten bronze (TB) symmetry [21,22]. The characteristic feature of the TTB (tetragonal tungsten bronze) crystal structure is that it consists of three types of tunnels (A, B, C) with different coordination numbers with the corner-shared octahedral formation. Owing to the different tunnel structures, the TTB structure allows for various RE substitutions in these channels or within the octahedral [23,24]. Different synthesis methods have been performed for the fabrication of $BaTa_2O_6$ such as co-precipitation, mechanochemical synthesis, ceramic flux and solid-state method [25–30]. $BaTa_2O_6$ has been reported in the literature with studies on its structural, dielectric, photocatalytic, thermodynamic and luminescence properties [31–44].

In this study, the tunability of $Tb^{3+}$ ion emission in the blue–green spectral region was investigated in detail. The structural and spectroscopic characterizations of $Tb^{3+}$ doped $BaTa_2O_6$ ceramic were carried out by using XRD, SEM-EDS, PL and decay time analyses. To our knowledge, this is the first report on the structural and optical properties of $Tb^{3+}$ doped $BaTa_2O_6$ crystals with a single phase.

Published online: 25 July 2023

## 2. Experimental

$BaCO_3$ ($\leq$ 99%, Sigma-Aldrich) and $Ta_2O_5$ (99.9%, Alfa Aesar) powders were used as starting materials for the synthesis of TTB-type $BaTa_2O_6$. $Tb_2O_3$ (99.9%, Alfa Aesar) powder was subsequently used as a dopant. The solid-state reaction method was used for the synthesis of both undoped and $Tb^{3+}$ doped $BaTa_2O_6$ ceramics. Initially, stoichiometric amounts of $BaCO_3$ and $Ta_2O_5$ powders were mixed well in an agate mortar to provide homogenization. Afterward, $x$ = 0.25–5 mol% $Tb_2O_3$ were added to the main mixture, where the $x$-value expresses 2 atomic values due to $Tb_2O_3$. Moreover, for further homogenization, oxide mixtures were stirred with an amount of acetone for 10 min. After that, the powder mixture was sintered in a high-temperature electric furnace at 1425°C for 20 h in an air atmosphere.

The crystalline structure of synthesized powders was characterized by X-ray diffractometer (XRD, Rigaku, D-MAX 2200 Model) using Cu $K_\alpha$ radiation ($2\theta$) between 15° and 60° at 2° $min^{-1}$ with a Ni filter. Microstructural properties and phase composition of the sintered samples were performed by scanning electron microscopy (SEM, JEOL, JSM-5910LV Model) with energy dispersive spectroscopy (EDS, Oxford, Inca x-Sight 7274 Model; 133-eV resolution 5.9 keV). For SEM-EDS analyses, the ceramic samples were coated with Au/Pd. PL (photoluminescence) emission, excitation and decay results were performed by a fluorescence spectrometer (FLS920, Edinburgh Instruments, UK) equipped with a 450 W ozone-free Xe lamp. In PL measurements, increment (step), dwell time, scan slit and detector type are 2 nm, 0.20 s, 2.4975 and red PMT steady state, respectively. Decay results were obtained using a time-dependent single-photon count device. The absorption spectrum of the $BaTa_2O_6$ sample was taken by using a Perkin-Elmer Lambda spectrophotometer (USA). All the measurements were taken at room temperature.

## 3. Results and discussion

### 3.1 *XRD and SEM-EDS analyses*

XRD results revealed a single $BaTa_2O_6$ phase (JCPDS card No.17-0793) from 0.25 to 5 mol% and no secondary phase was observed in the powders (figure 1). The powders crystallized in tetragonal symmetry with space group *P*4/*mbm* having the tetragonal tungsten bronze (TTB) type structure, in which the cell parameters are $a$ = 12.52 Å, $c$ = 3.956 Å and $V$ = 620.10 (Å)$^3$ [21]. For oxide compounds, TTB-type structure can be described as the $A_4B_2C_4M_{10}O_{30}$ formula, where the pentagonal A, square B sites (for large cations) and triangular C sites (for small cations) are 15, 12 and 9 CN, respectively, while small and highly charged cations are in octahedral M sites (M = Nb, Ta, Mo, W) with 6 CN [36–44]. Based on the ionic radius and valence, $Tb^{3+}$ ions may occupy the A and B tunnels of TTB structure, which have an ionic radius of 1.095 Å (9 of CN) compared to $Ba^{2+}$ ions, 1.61 Å (12 of CN). The pentagonal A tunnels in the structure are more likely to be occupied by $Ba^{2+}$ ions than square B tunnels in terms of coordination number and ionic radius. On the other hand, although the tetragonal polymorph with a TTB structure is formed between 1150 and 1300°C, it can remain kinetically stable at high temperatures (e.g., 1550°C) [29]. The charge balance of the structure may change with $Tb^{3+}$ doping, but the stable TTB tunnel structure of the samples fabricated at 1425°C probably prevented the formation of the secondary phase at the high sintering temperature. In addition, studies in which the single-phase structure is preserved at higher RE concentrations have been reported [39,40]. Moreover, the increase in concentration in the $Eu^{3+}$ doped $BaTa_2O_6$ structure and the orientation from the centrosymmetric (B) to the non-centrosymmetric pentagonal (A) sites are associated with the PL asymmetry ratio [39].

Figure 2 shows SEM images of undoped, 0.5, 1 and 5 mol% $Tb^{3+}$ doped $BaTa_2O_6$ powders. As seen in the SEM images, the morphology of the grains was affected by the $Tb^{3+}$ concentration. The grains of the undoped sample had amorphous and roundish, while the grain size of the $Tb^{3+}$ doped samples decreased with the increase in concentration and became slightly cornered. The grain sizes for the undoped and 0.5, 1, 5 mol% $Tb^{3+}$ doped samples ranged from 0.5–5, and 0.5–3, 0.4–2, 0.3–1.5 μm, respectively. The decrease in grain size with the increase in $Tb^{3+}$ concentration may be ascribed to the restriction of grain growth because of lattice suppression [36,41]. SEM-EDS analysis of 5 mol% $Tb^{3+}$ doped powder was shown in figure 3. EDS analysis revealed that the elemental (at%, wt%) compositions agree with the theoretical (theo. at%) compositions.

### 3.2 *Photoluminescence properties and quantum efficiency*

Figure 4 shows the absorption spectrum of the tetragonal $BaTa_2O_6$ host. As seen in the spectrum, $BaTa_2O_6$ exhibits host absorption around 300 nm. Kato and Kudo [33] studied PL of the $BaTa_2O_6$ host, where the excitation and emission of tetragonal $BaTa_2O_6$ were 303 and 500 nm, respectively. Kato and Kudo [28,33] determined the bandgap energy for tetragonal $BaTa_2O_6$ as 3.8 eV, which is close to the value determined in this study. Moreover, İlhan and Güleryüz [43] reported the cathodoluminescence of $Sm^{3+}$ doped tetragonal $BaTa_2O_6$, where the host emission exhibits a peak of 495 nm. In addition, İlhan *et al* [23] revised the CT transition of $Eu^{3+}$ doped tetragonal $BaTa_2O_6$ at about 330 nm.

Figure 5 shows the PL excitation spectra of 0.5 mol% $Tb^{3+}$ doped $BaTa_2O_6$ phosphors, where a broad and intense band near 321.7 nm is assigned to the $4f^8 \rightarrow 4f^75d$ transition of $Tb^{3+}$. However, the broad excitation band of the phosphor cannot be attributed to the $O^{2-} \rightarrow Tb^{3+}$ charge-transfer (CT) transition because the CT states have much

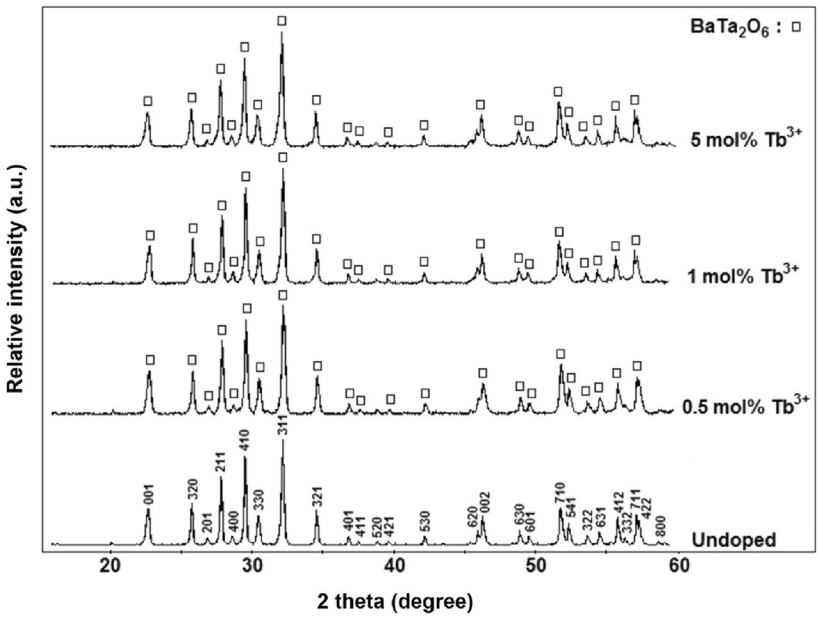


**Figure 1.** X-ray diffractions of undoped and $Tb^{3+}$ doped $BaTa_2O_6$ samples.

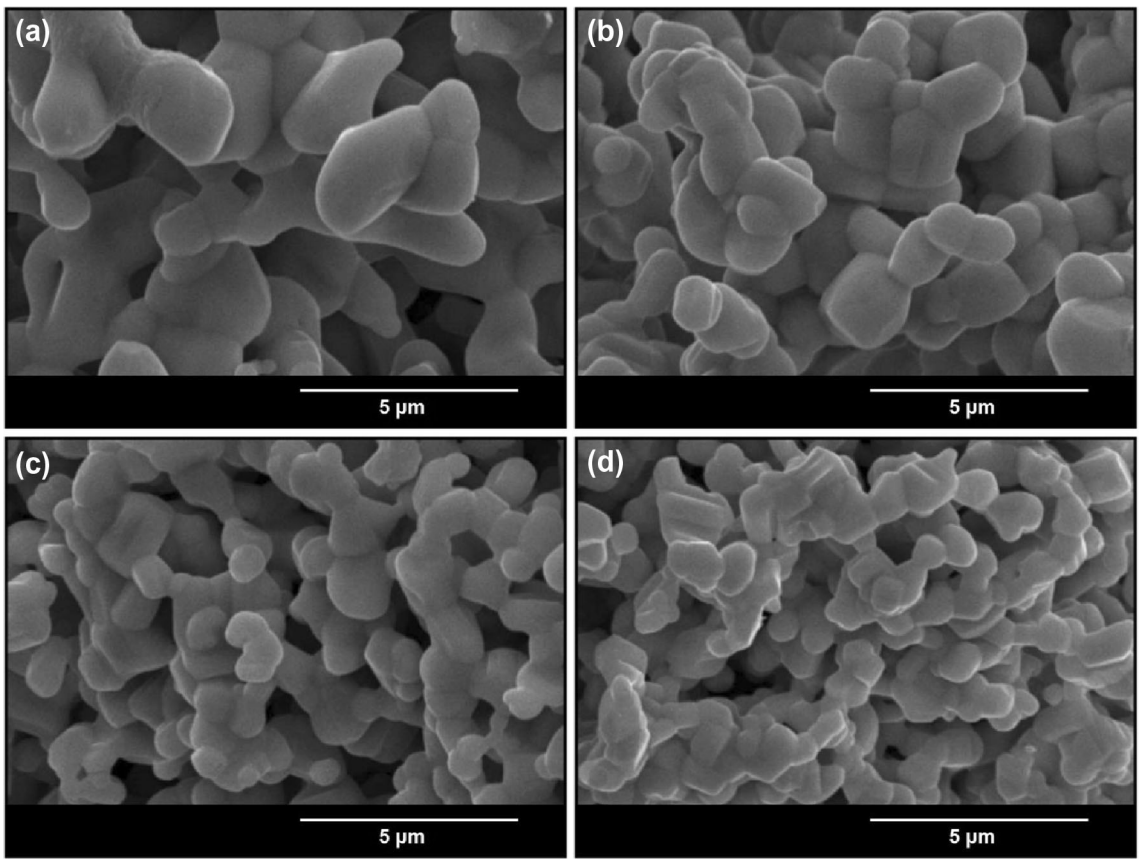


**Figure 2.** SEM micrographs: (**a**) undoped, (**b**) 0.5 mol%, (**c**) 1 mol% and (**d**) 5 mol% $Tb^{3+}$ doped samples at 10.000× magnification using 20 kV acceleration voltage.

higher energy (60.000 $cm^{-1}$) than 5d states of $Tb^{3+}$ [12,45]. PL spectra of the phosphors with excitation of 321.7 nm are given in figure 6. The spectra of the $Tb^{3+}$ transitions ($^5D_3 \rightarrow {}^7F_J$) in the blue region are $^5D_3 \rightarrow {}^7F_6$ (379.8 nm), $^5D_3 \rightarrow {}^7F_5$ (413.4 nm), $^5D_3 \rightarrow {}^7F_4$ (435.7 nm), $^5D_3 \rightarrow {}^7F_3$ (455.6 nm), $^5D_3 \rightarrow {}^7F_2$ (474.5 nm). The spectra

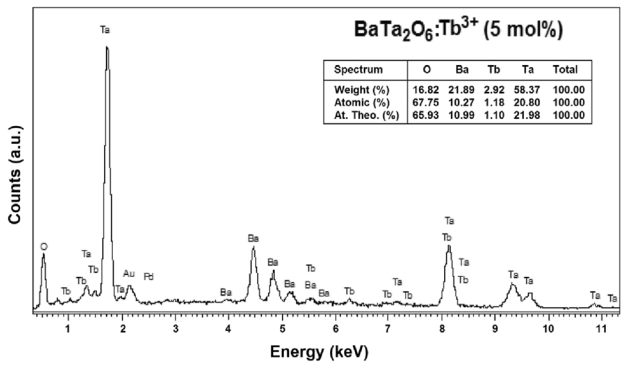


**Figure 3.** EDS spectrum and wt%, at% and theoretical at% values for 5 mol% $Tb^{3+}$ doped $BaTa_2O_6$ sample.

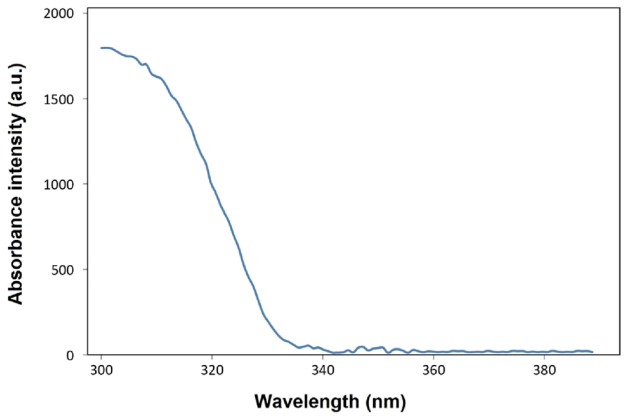


**Figure 4.** Absorbance spectrum of tetragonal $BaTa_2O_6$.

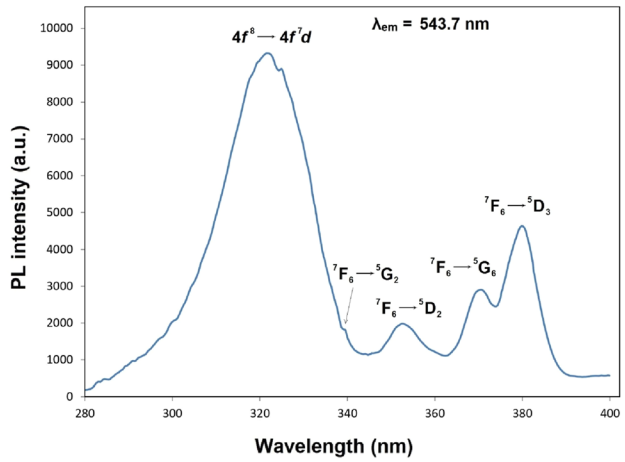


**Figure 5.** PL excitation spectrum of 0.5 mol% $Tb^{3+}$ doped $BaTa_2O_6$ using 543.7 nm emission.

of $Tb^{3+}$ transitions in green region are $^5D_4 \rightarrow {}^7F_6$ (487.9 nm), $^5D_4 \rightarrow {}^7F_5$ (543.7 nm), $^5D_4 \rightarrow {}^7F_4$ (583.4 nm), $^5D_4 \rightarrow {}^7F_3$ (621.3 nm). Among all the phosphors, the highest emission intensity with excitation of 543.7 nm was observed for the 0.5 mol% $Tb^{3+}$ doped sample (figure 6). The concentration quenching occurring over 0.5 mol% is associated with the non-radiative energy transfer due to the

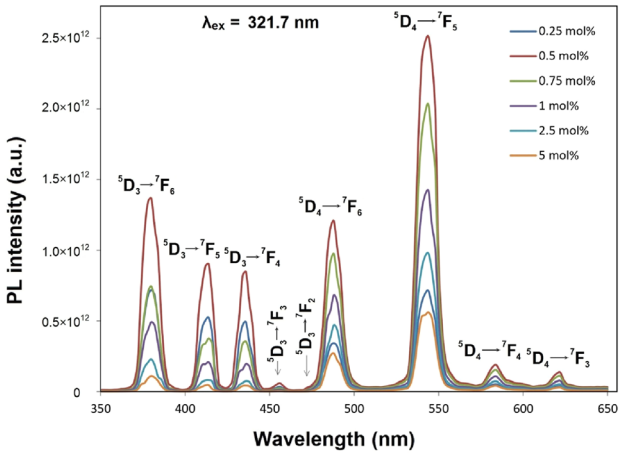


**Figure 6.** PL spectra of $BaTa_2O_6:Tb^{3+}$ with excitation of 321.7 nm.

shortening of the $RE^{3+}$–$RE^{3+}$ distance at high $RE^{3+}$ concentrations, and this phenomenon occurs two ways; the transfer of excitation energy between the dopant ions and the increase in electronic defect levels. Therefore, the decreasing distance between $Tb^{3+}$–$Tb^{3+}$ ions would be accelerated for the non-radiative energy transfer. Accordingly, the critical distance ($R_c$) for the concentration quenching in the energy transfer between $Tb^{3+}$–$Tb^{3+}$ ions can be estimated from equation (1) [46]:

$$R_c \approx 2\left(\frac{3V}{4\pi X_c N}\right)^{1/3} \quad (1)$$

where $V$ is the lattice volume, $X_c$ is the critical concentration of $RE^{3+}$ ion, and $N$ (or $Z$) is the number of host cations in the unit cell. The $V$ and $N$ values for $BaTa_2O_6$ are 620.10 $A^3$, and 5, respectively. The $R_c$ (critical concentration) of $Tb^{3+}$ is 0.01 (for 0.5 mol% $Tb_2O_3$). So, the $R_c$ of $Tb^{3+}$–$Tb^{3+}$ ions is determined to be 28.72 Å. The critical distance of $Tb^{3+}$–$Tb^{3+}$ calculated in the study and the critical distances of other $BaTa_2O_6:RE^{3+}$ phosphors are summarized in table 1. The $Tb^{3+}$–$Tb^{3+}$ distance is more than 5 (Å), which can be attributed to the multipolar

**Table 1.** Comparative critical distances of $BaTa_2O_6:RE^{3+}$ (RE = Tb, Nd, Er, Dy, Eu, Sm, Pr, Ho) phosphors.

| Phosphor | Critical distance ($R_c$), Å | References |
|---|---|---|
| $BaTa_2O_6:Tb^{3+}$ | 28.72 | This study |
| $BaTa_2O_6:Nd^{3+}$ | 16.80 | [41] |
| $BaTa_2O_6:Er^{3+}$ | 8.40 | [42] |
| $BaTa_2O_6:Dy^{3+}$ | 10.58 | [40] |
| $BaTa_2O_6:Eu^{3+}$ | 7.34 | [39] |
| $BaTa_2O_6:Sm^{3+}$ | 16.80 | [37] |
| $BaTa_2O_6:Pr^{3+}$ | 19.92 | [38] |
| $BaTa_2O_6:Ho^{3+}$ | 16.80 | [36] |

interaction mechanism or ineffectiveness of the exchange interaction mechanism [47]. As seen in the table, other reported phosphors also have multipolar interaction mechanism. The interaction type of energy transfer mechanism can be estimated by Van Uitert's theory [48]. According to this theory, the type of the multipolar interaction mechanism can be found from the change of the emission intensity and ion concentration in case of the energy transfer takes place between the same type of dopant, which follows equation (2):

$$I/x = K\left[1+\beta(x)^{\theta/3}\right]^{-1} \tag{2}$$

where $\theta$ is the character of the multipolar interaction, $x$ is the RE concentration, $I/x$ is a ratio of the emission intensity ($I$) to phosphor concentration ($x$), and the $K$ and $\beta$ constants are of the phosphor at the same excitation wavelength. The $\theta = 3$ parameter indicates the electric multipolar property where the energy transfer among the nearest-neighbour ions is the exchange interaction. The $\theta = 6$, $\theta = 8$ and $\theta = 10$ values are the dipole–dipole (d–d), dipole–quadrupole (d–p) and quadrupole–quadrupole (q–q) interactions, respectively. In equation (2), accepting the $\beta(x)^{\theta/3} >> 1$, the modified form can be given as equation (3):

$$\log(I/x) = K' - \theta/3 \log x \quad (K' = \log K - \log \beta) \tag{3}$$

The $\theta$ parameter can be estimated from the slope of equation (3) which is plotted between the log ($I/x$) and log ($x$). The graph of log ($I/x$) as a function of log ($x$) for $BaTa_2O_6$:$Tb^{3+}$ phosphors is given in figure 7. The critical concentration of $Tb^{3+}$ was taken as $x \geq 0.01$ (0.5 mol% $Tb_2O_3$). This plot shows the dependence of log ($I/x$) on log ($x$) of $Tb^{3+}$ where the estimated value of the slope is about − 1.4931. The $\theta$ value was determined as 4.48, which is close to 6. Consequently, the energy transfer mechanism of the phosphor can be ascribed to the dipole–dipole (d–d) interaction.

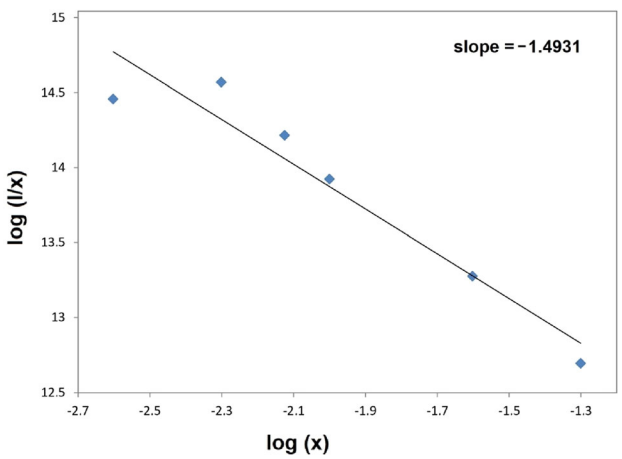


**Figure 7.** Relation between the $\log_{10}(I/x)$ and $\log_{10}(x)$ of $BaTa_2O_6$:$Tb^{3+}$ phosphors.

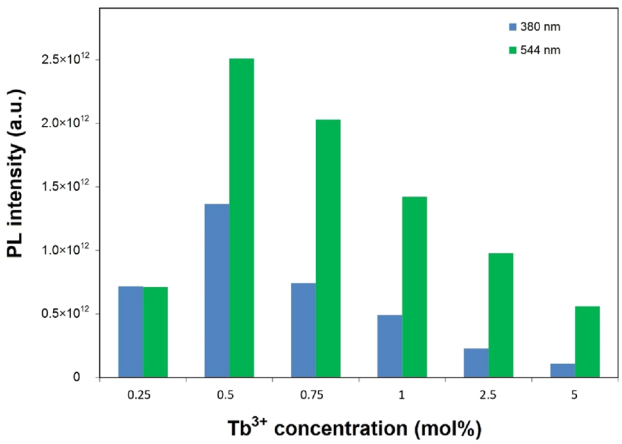


**Figure 8.** Relative emission intensity of $^5D_4$ and $^5D_3$ transitions depending on the $Tb^{3+}$ concentration.

Figure 8 shows the relative emission intensity of $^5D_4$ and $^5D_3$ transitions, where $^5D_3$ decreases as $^5D_4$ increases depending on the increase in $Tb^{3+}$ concentration. The $^5D_3$ state can be associated with two opposite effects. First, the decreasing number of luminescence centres with decreasing $Tb^{3+}$ concentration tends to decrease the relative emission intensity. Second, the relative emission intensity of the $^5D_3$ increases with the decrease in $Tb^{3+}$ concentration, because of the cross-relaxation effect which quenches the $^5D_3$ state at a lower doping concentration [10–13]. Thus, the relative emission intensity of the $^5D_3$ state does not lead to a regular trend like the $^5D_4$ state, due to these two effects occurring in opposite directions. However, there is an exponential trend between the PL emission intensity ratio of $^5D_3 \rightarrow {}^7F_5$ and $^5D_4 \rightarrow {}^7F_5$ transitions depending on $Tb^{3+}$ concentration, which is given in figure 9. The emission intensity decrease of $^5D_3 \rightarrow {}^7F_J$ and emission intensity increase of $^5D_4 \rightarrow {}^7F_J$ with the increase in $Tb^{3+}$ concentration are depending on

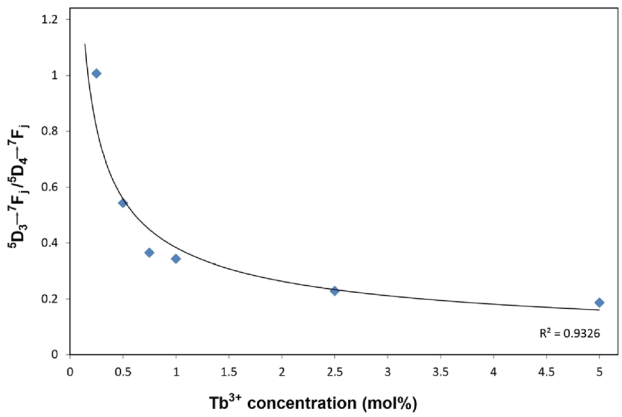


**Figure 9.** PL emission intensity ratio of $^5D_3 \rightarrow {}^7F_5$ and $^5D_4 \rightarrow {}^7F_5$ transitions depending on $Tb^{3+}$ concentration.

the cross-relaxation and this phenomenon can be expressed by equation (4) [10,11]:

$$Tb^{3+}\left[{}^5D_3\right] + Tb^{3+}\left[{}^7F_6\right] \rightarrow Tb^{3+}\left[{}^5D_4\right] + Tb^{3+}\left[{}^7F_0\right] \tag{4}$$

The $^5D_3 \rightarrow {}^7F_J$ and $^5D_4 \rightarrow {}^7F_J$ emissions and the cross-relaxation mechanism resulting from the excitation of $^5D_3$ and $^5D_4$ energy levels are given in figure 10. The chromaticity coordinates of $BaTa_2O_6$:$Tb^{3+}$ phosphor in the CIE (Commission Internationale de I'Eclairage) diagram depending on $Tb^{3+}$ concentration are shown in figure 11. The emission of phosphor shows a trend from blue (low doping concentration) to green (high doping concentration) with the increase in $Tb^{3+}$ concentration. Accordingly, the $Tb^{3+}$ emission can be adjusted from the blue region to the green region with increasing $Tb^{3+}$ concentration in the CIE diagram.

Figure 12a and b shows the decay curves of $BaTa_2O_6$:$Tb^{3+}$ phosphors for $^5D_3$ and $^5D_4$ states, respectively. The curves of the average decay time ($\tau$) or observed lifetime can be expressed as dual temporal dependence in equation (5) [23]:

$$I^{L}_{(t)} = I^{L}_{(0)} + B_1 \exp\frac{t_0 - t}{\tau_1} + B_2 \exp\frac{t_0 - t}{\tau_2} \tag{5}$$

where $I^{L}_{(t)}$ and $I^{L}_{(0)}$ are the PL intensities, $B_1$ and $B_2$ are the fitting constants, the long and short lifetimes for exponential components are $\tau_1$ and $\tau_2$, respectively. The observed lifetime ($\tau$) can be determined by equation (6) according to the variables in equation (5) [23]:

$$\tau = \frac{B_1\tau_1^2 + B_2\tau_2^2}{B_1\tau_1 + B_2\tau_2} \tag{6}$$

The observed lifetimes for $^5D_3$ and $^5D_4$ states are given in table 2 and the observed lifetimes of $^5D_3 \rightarrow {}^7F_5$ and $^5D_4 \rightarrow {}^7F_5$ transitions depending on $Tb^{3+}$ concentration is given in figure 13. The observed lifetimes of $^5D_3$ and $^5D_4$ states for 0.25 and 5 mol% varied from 14.13 and 11.02 µs to 9.16 and 10.81 µs, respectively. The lowest mol% ratio

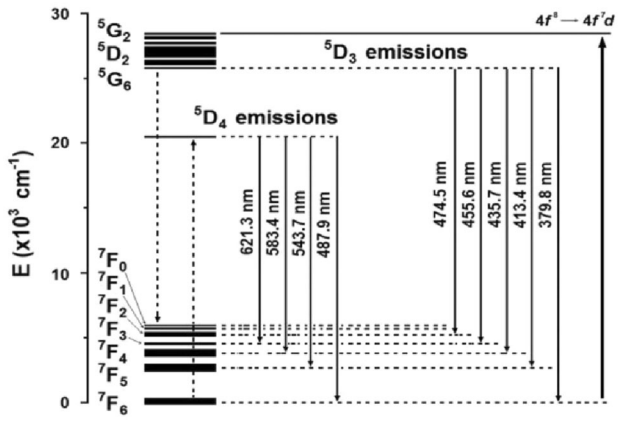


**Figure 10.** Partial energy level diagram of $Tb^{3+}$ ion and scheme of cross-relaxation process.

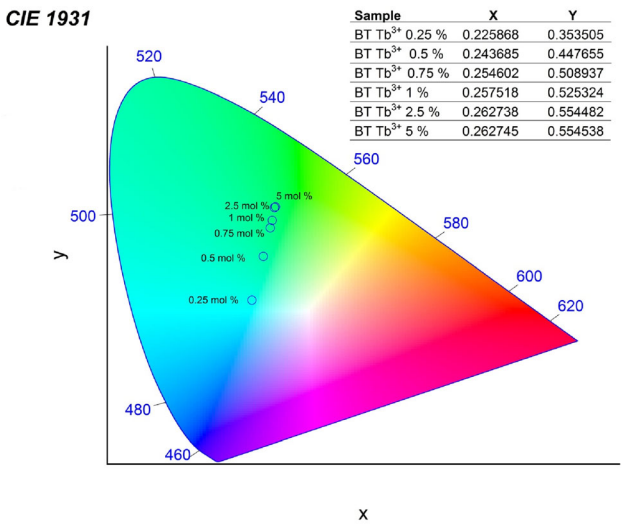


**Figure 11.** CIE chromaticity coordinates of $BaTa_2O_6$:$Tb^{3+}$ phosphor.

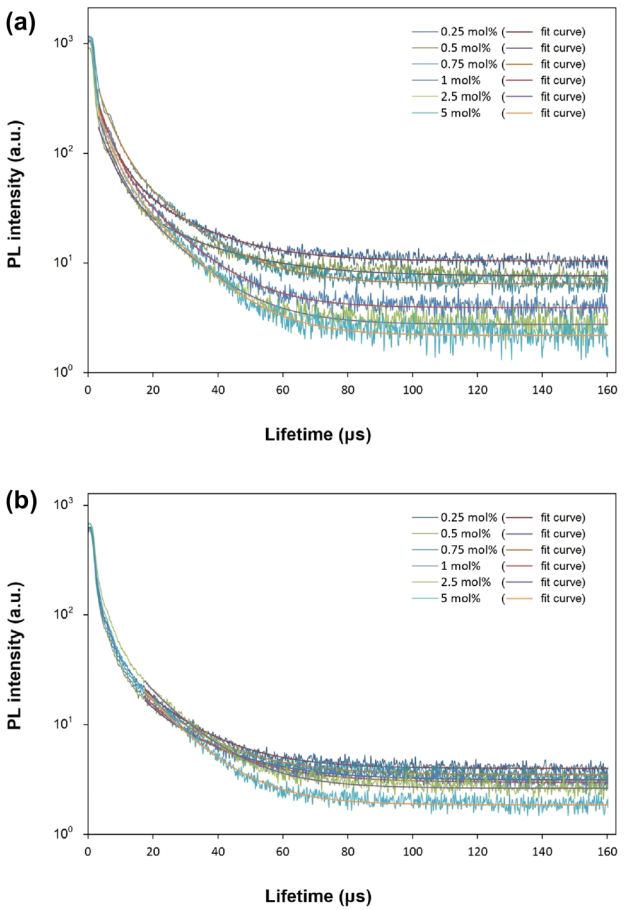


**Figure 12.** Decay curves and fit curves of $BaTa_2O_6$:$Tb^{3+}$ phosphors for (**a**) $^5D_3$ and (**b**) $^5D_4$ states.

in the study is 0.25. An extrapolation was used to determine the mole ratio (0.01 mol%) closest to the zero value. The decay times of the phosphor for the lowest $Tb^{3+}$ concentration ($\tau_{10}$) was fitted to be 22.00 µs (for $^5D_3$) and 11.02 µs

**Table 2.** $Tb^{3+}$–$Tb^{3+}$ critical distance ($R_c$), $^5D_3$ and $^5D_4$ lifetimes ($\tau$), cross-relaxation rate ($W_{CR}$), cross-relaxation efficiency ($\eta_{CR}$), radiative ($A_r$), non-radiative ($A_{nr}$) and total ($A_r + A_{nr}$) rates, and $^5D_3$ state quantum efficiency ($\eta_{QE}$) for all Tb-doped phosphors.

| $Tb^{3+}$ conc. (mol%) | $R_c$ (Å) | $\tau$ ($^5D_3$) (μs) | $\tau$ ($^5D_4$) (μs) | $W_{CR}$ (m $s^{-1}$) | $\eta_{CR}$ (%) | $W_0$ (m $s^{-1}$) | $A_{nr} + A_r$ (m $s^{-1}$) | $A_{nr}$ (m $s^{-1}$) | $A_r$ (m $s^{-1}$) | $\eta_{QE}$ (%) |
|---|---|---|---|---|---|---|---|---|---|---|
| 0.01 | 105.82 | 22.00 | 11.02 | 0.000 | 0.00 | 3.970 | 45.45 | 0.00 | 45.45 | 100.00 |
| 0.25 | 36.19 | 14.13 | 10.86 | 25.325 | 35.78 | 2.126 | 70.78 | 27.16 | 43.62 | 61.63 |
| 0.5 | 28.72 | 13.29 | 10.93 | 29.812 | 39.61 | 1.349 | 75.27 | 30.97 | 44.29 | 58.85 |
| 0.75 | 25.09 | 10.39 | 11.11 | 50.809 | 52.78 | 1.544 | 96.26 | 52.14 | 44.12 | 45.84 |
| 1 | 22.80 | 9.86 | 11.17 | 55.927 | 55.16 | 1.598 | 101.38 | 57.30 | 44.08 | 43.48 |
| 2.5 | 16.80 | 9.41 | 10.74 | 60.798 | 57.22 | 1.158 | 106.25 | 61.80 | 44.46 | 41.84 |
| 5 | 13.33 | 9.16 | 10.81 | 63.724 | 58.37 | 0.990 | 109.18 | 64.58 | 44.60 | 40.85 |

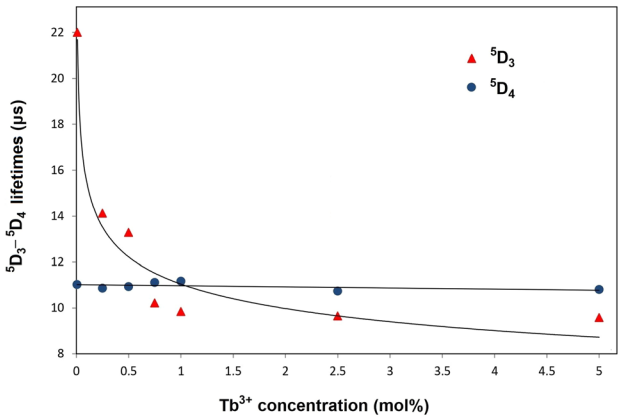


**Figure 13.** Observed lifetimes of $^5D_4$ and $^5D_3$ transitions depending on the $Tb^{3+}$ concentration.

(for $^5D_4$), where $\tau_{10}$ represents the intercept of the plot of decay time *vs.* $Tb^{3+}$ ions doping concentration when $x = 0.01$ mol%. All the PL decay profiles of the $^5D_3$ and $^5D_4$ states are double exponential. With the increase in $Tb^{3+}$ concentration, the observed lifetimes of the $^5D_3$ state decrease while the decay profiles of the $^5D_4$ state tend to be straight. This is mainly due to cross-relaxation depending on the $Tb^{3+}$ concentration and can be attributed to the process of $Tb^{3+}$ [$^5D_3$] + $Tb^{3+}$ [$^7F_6$] → $Tb^{3+}$ [$^5D_4$] + $Tb^{3+}$ [$^7F_0$]. In the $Tb^{3+}$ luminescence, the decay time of blue emission ($^5D_3$) is affected rapidly by the shortening of the distance between $Tb^{3+}$ and $Tb^{3+}$, while the decay time of green emission ($^5D_4$) can remain stable. It is likely that non-radiative energy transfer is effective for $^5D_3$, which decreases rapidly with the increase of $Tb^{3+}$ during cross-relaxation. Accordingly, hardly changing decay times in the $^5D_4$ transition can be attributed to the suppression of the non-radiative energy for this transition. The similar results are reported in the literature [10,11]. The cross-relaxation ($W_{CR}$) rate and cross-relaxation efficiency ($\eta_{CR}$) can be directly determined from the observed lifetime parameters by using equations (7 and 8), respectively,

$$W_{CR} = \frac{1}{\tau_1} - \frac{1}{\tau_{10}} \tag{7}$$

$$\eta_{CR} = 1 - \frac{\tau_1}{\tau_{10}} \tag{8}$$

where $\tau_1$ is any concentration value of $^5D_3$ state lifetime, $\tau_{10}$ is the 0.01 mol% $Tb^{3+}$ concentration value of $^5D_3$ state lifetime. Figures 14 and 15 show the $W_{CR}$ and $\eta_{CR}$ increase with increasing $Tb^{3+}$ concentration, respectively. The increase of $W_{CR}$ and $\eta_{CR}$ parameters with the decrease of distance between the $Tb^{3+}$ ions depending on the increase of $Tb^{3+}$ concentration are tabulated in table 2. The relationship between $W_{CR}$ and $Tb^{3+}$ concentrations can be expressed by equation (9):

$$W_{CR} = A\ln x + c \tag{9}$$

where $A$ is a constant, and $x$ is $Tb^{3+}$ mol% concentration. Accordingly, $\tau_{10}$ can be presented by equation (10) [10,11]:

$$\tau_{10} = \frac{1}{W_0 + A_r} \tag{10}$$

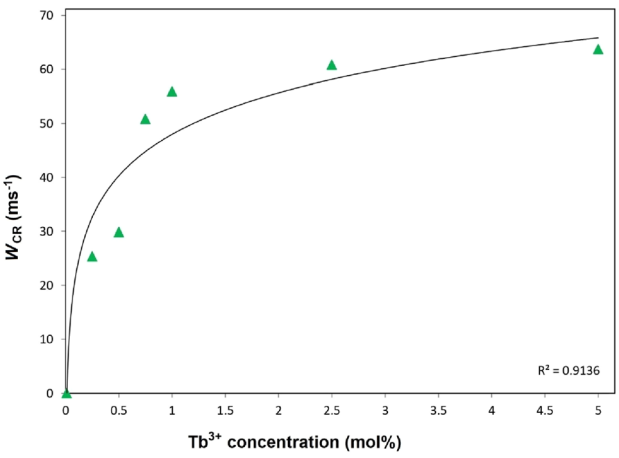


**Figure 14.** Cross-relaxation ($W_{CR}$) change with $Tb^{3+}$ concentration.

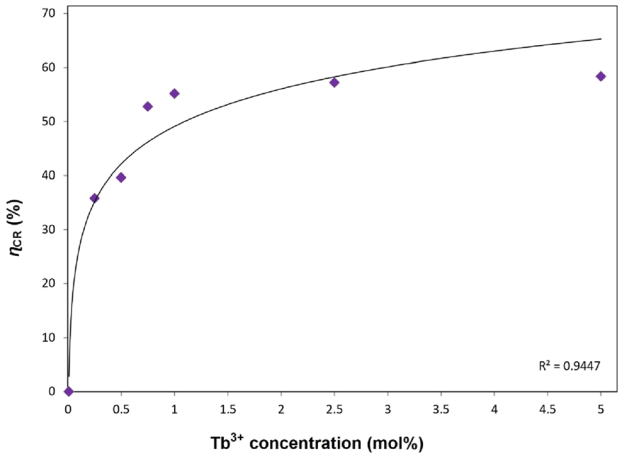


**Figure 15.** Cross-relaxation efficiency ($\eta_{CR}$) change with $Tb^{3+}$ concentration.

where $W_0$ is the multiphonon rate and $A_r$ is the radiative transition rate of $^5D_3$. The $W_0$ and $A_r$ are independent of $Tb^{3+}$ concentration. Therefore, by substituting equations (7 and 9) in equation (10), as stated in equation (11), a relationship can be established between $\tau_1$ and $Tb^{3+}$ concentration, that is $B = W_0 + A_r$. Accordingly, the $\tau_1$ graphic as a function of $x$ is given in figure 13, which can be fitted by using equation (11) for the determination of $B$-value.

$$\tau_1 = \frac{1}{Ax + B} \tag{11}$$

There is a ratio between the green and blue emissions of $Tb^{3+}$ and this ratio is related to the green–blue spectral region emission intensities, which are given by equation (12) [10,11]:

$$\frac{R_{G/B}}{R_0} = 1 + \frac{W_{CR}}{W_0} \tag{12}$$

where $R_{G/B}$ is the ratio of green and blue, which can be obtained for different $Tb^{3+}$ concentrations directly from the emission spectra. The $R_0$ is the ratio between the green and blue emissions for the 0.01 mol%-doped sample. Accordingly, as seen in figure 16, a graphic of $R_{G/B}/R_0$ *vs.* $W_{CR}$ is plotted and it was used to determine the $W_0$ value. So that, the quantum efficiency ($\eta_{QE}$) of the $^5D_3$ excited level can be found from the $W_{CR}$, $W_0$ and $\tau_1$ parameters, applying equations (13, 14 and 15) [10,11]:

$$\eta_{QE} = \frac{A_r}{A_r + A_{nr}} \tag{13}$$

$$A_{nr} = W_{CR} + W_0 \tag{14}$$

$$A_r + A_{nr} = \frac{1}{\tau} \tag{15}$$

where $\eta_{QE}$ is the quantum efficiency of $^5D_3$ level for $Tb^{3+}$ ion, $A_r$ and $A_{nr}$ are the radiative and non-radiative values, respectively. The results are summarized in table 2. The quantum efficiency of the $^5D_3$ state is relatively high for the low $Tb^{3+}$ doping concentrations, and so the quantum efficiency decreased with the increase of $Tb^{3+}$ concentration depending on the cross-relaxation phenomenon where the $Tb^{3+}$–$Tb^{3+}$ distance is shortening.

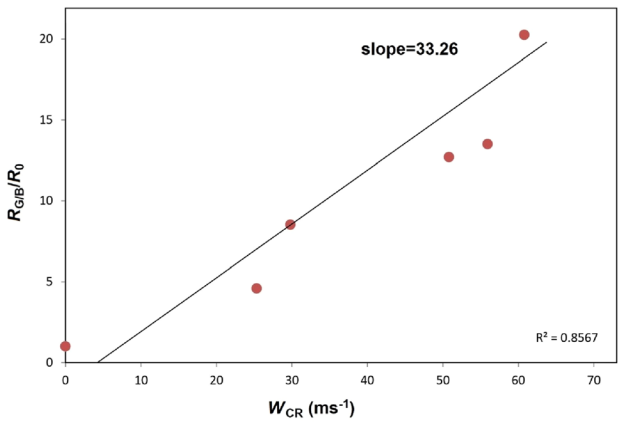


**Figure 16.** Plot of variation of $R_{G/B}/R_0$ and $W_{CR}$.

## 4. Conclusions

$Tb^{3+}$ doped TTB-type $BaTa_2O_6$ with a single phase was synthesized by the solid-state route. XRD findings indicated TTB-type crystal structure with a single phase for 0.25–5 mol% $Tb^{3+}$ doping concentrations. SEM examination showed a decrease in $BaTa_2O_6$ grain size with increasing $Tb^{3+}$ concentration. While PL emission intensity increased between 0.25 and 0.5 mol%, the luminescence of phosphor reached the maximum level for 0.5 mol% $Tb^{3+}$ and then the concentration quenching occurred. The PL emissions with increasing concentration of $Tb^{3+}$ changed from blue to green due to the cross-relaxation process, which is associated with the emission colour tunability. In the CIE diagram, the PL emission of phosphor shifted from the blue region to the green region with increasing $Tb^{3+}$ concentration. While the distance between $Tb^{3+}$ ions decreased with the increase in $Tb^{3+}$ concentration, $W_{CR}$ and $\eta_{CR}$ parameters increased. The observed lifetimes of the $^5D_3$ state due to cross-relaxation decreased depending on the $Tb^{3+}$ concentration, while the decay profiles of the $^5D_4$ state tended to be flat. Consequently, $BaTa_2O_6$:$Tb^{3+}$ phosphor with its tunable emission colour properties from blue to green may be a good candidate for photonic applications.

## References

[1] Bharathi N V, Kavitha P, Ramaswamy S, Jayabalakrishnan S S and Sakthipandi K 2022 *Bull. Mater. Sci.* **45** 172
[2] Ramteke S K, Yerpude A N, Kokode N S and Dhoble S J 2021 *Bull. Mater. Sci.* **44** 174
[3] İlhan M, Keskin İÇ and Gültekin S 2020 *J. Electron. Mater.* **49** 2436

[4] Palan C B, Bajaj N S, Soni A and Komanwar S K 2016 *Bull. Mater. Sci.* **39** 1157
[5] Du Z, Liu Q, Hou T, Song Y, Zhang X and Cui Y 2015 *Bull. Mater. Sci.* **38** 805
[6] Yerpude A N and Dhoble S J 2013 *Bull. Mater. Sci.* **36** 715
[7] Palan C B, Bajaj N S, Soni A, Kulkarni M S and Komanwar S K 2015 *Bull. Mater. Sci.* **39** 1527
[8] Li Y C, Chang Y H, Lin Y F, Chang Y S and Lin Y 2006 *J. Electrochem. Solid State* **9** H74
[9] Verma R K, Kumar K and Rai S B 2010 *Solid State Sci.* **12** 1146
[10] Bispo-Jr A G, Lima S A M, Lanfredi S, Praxedes F R and Pires A M 2019 *J. Lumin.* **214** 116604
[11] Hao Z, Zhang J, Zhang X, Lu S and Wanga X 2009 *J. Electrochem. Soc.* **156** 193
[12] Boruc Z, Fetlinski B, Kaczkan M, Turczynski S, Pawlak D and Malinowski M 2012 *J. Alloys Compd.* **532** 92
[13] Liu X, Pang R, Quan Z, Yang J and Lin J 2007 *J. Electrochem. Soc.* **154** J185
[14] Fu Y and Hu Y 2015 *Mater. Sci. Mater. Electron.* **27** 3867
[15] Shon K S and Shin N 2002 *Electrochem. Solid State Lett.* **5** H21
[16] Robbins D, Cockayne B, Lent B and Glasper J 1976 *Solid State Commun.* **20** 673
[17] Ronda C R, Jüstel T and Nikol H 1998 *J. Alloys Compd.* **275–277** 669
[18] Raju G S R, Pavitra E, Nagaraju G, Guan X Y and Yu J S 2015 *RSC Adv.* **5** 22217
[19] Ratnam B, Jayasimhadri M, Kumar G B, Jang K, Kim S, Lee Y *et al* 2013 *J. Alloys Compd.* **564** 100
[20] dos Santos J F M, Terra I A A, Astrath N G C, Guimarães F B, Baesso M L, Nunes L A O *et al* 2015 *J. Appl. Phys.* **117** 053102
[21] Layden G K 1967 *Mater. Res. Bull.* **2** 533
[22] Layden G K 1968 *Mater. Res. Bull.* **3** 349
[23] İlhan M, Katı M İ, Keskin İÇ and Güleryüz L F 2022 *J. Alloys Compd.* **901** 163626
[24] Simon A and Ravez J 2006 *C. R. Chim.* **9** 1268
[25] Navale S C, Samuel V, Gaikwad A B and Ravi V 2007 *Ceram. Int.* **33** 297
[26] İlhan M, Mergen A and Yaman C 2011 *Ceram. Int.* **37** 1507
[27] İlhan M, Mergen A and Yaman C 2013 *Ceram. Int.* **39** 5741
[28] Kato H and Kudo A 2003 *Catal. Today* **78** 561
[29] Vanderah T A, Roth R S, Siegrist T, Febo W, Loezos J M and Wong-Ng W 2003 *Solid State Sci.* **5** 149
[30] Zhang W, Kumada N, Takei T, Yamanaka J and Kinomura N 2005 *Mater. Res. Bull.* **40** 1177
[31] Mumme W G, Grey I E, Roth R S and Vanderah T A 2007 *J. Solid State Chem.* **180** 2429
[32] Lee Y H, Kim Y S, Kim D H and Oh M H 2000 *IEEE Trans. Electron Devices* **47** 71
[33] Kato H and Kudo A 1998 *Phys. Lett.* **295** 487
[34] İlhan M, Mergen A, Sarıoğlu C and Yaman C 2017 *J. Therm. Anal. Calorim.* **128** 707
[35] Ekmekçi M K, İlhan M, Güleryüz L F and Mergen A 2017 *Optik* **128** 26
[36] İlhan M 2014 *Solid State Sci.* **38** 160
[37] Ekmekçi M K, İlhan M, Başak A S and Deniz S 2015 *J. Fluoresc.* **25** 1757
[38] İlhan M, Samur R, Demirer H and Mindivan F 2015 *Metabk* **54** 407
[39] İlhan M, Ekmekçi M K, Mergen A and Yaman C 2016 *J. Fluoresc.* **26** 1671
[40] İlhan M, Ekmekçi M K, Mergen A and Yaman C 2017 *J. Appl. Ceram. Technol.* **14** 1134
[41] İlhan M, Keskin İÇ, Çatalgöl Z and Samur R 2018 *J. Appl. Ceram. Technol.* **15** 1594
[42] İlhan M 2017 *AKU J. Sci. Eng.* **17** 675
[43] İlhan M and Güleryüz L F 2022 *Chem. Pap.* **76** 6963
[44] İlhan M, Keskin İÇ, Güleryüz L F and Katı M İ 2022 *Mater. Sci. Mater. Electron.* **33** 16606
[45] Nugent L J, Baybarz R D, Burnett J L and Ryan J L 1973 *J. Phys. Chem.* **77** 1528
[46] Blasse G 1986 *Solid State Chem.* **62** 207
[47] Blasse G 1969 *Philips Res. Rep.* **24** 131
[48] Van Uitert L G 1967 *J. Electrochem. Soc.* **114** 1048